RSC Advances

PAPER

View Article Online
View Journal | View Issue

Cite this: *RSC Adv.*, 2024, **14**, 25369

Crystallization of smooth amorphous calcium phosphate microspheres to core–shell hydroxyapatite microspheres†

Mei-li Qi,[ab] Zhaoxuan Long,[a] Xiao-Cun Liu,[ab] Haijun Zhang,[c] Jin Li*[ab] and Shengkun Yao*[de]

Received 4th June 2024
Accepted 7th August 2024

DOI: 10.1039/d4ra04078c

rsc.li/rsc-advances

Calcium phosphates (Ca-P) represent a significant class of biological minerals found in natural hard tissues. Crystallization through phase transformation of a metastable precursor is an effective strategy to guide the growth of crystalline Ca-P with exceptional functionality. Despite extensive research on Ca-P, the exact process during the crystallization of amorphous particles to hydroxyapatite (HA) remains elusive. Herein, pure HA microspheres with a core–shell structure are crystallized *via* dissolution and re-crystallization of smooth amorphous calcium phosphate (ACP) microspheres. The transformation is initiated with the increase of the hydrothermal treatment time in the presence of sodium trimetaphosphate and L-glutamic. The underlying mechanisms along with the kinetics of such transformation are explored. Nanocrystalline areas are formed on the smooth ACP microspheres and crystallization advances *via* nanometre-sized clusters formed by directional arrangement of nanocrystalline whiskers. Our findings shed light on a crucial but unclear stage in the genesis of HA crystals, specifically under the conditions of hydrothermal synthesis.

1. Introduction

Calcium phosphates (Ca-P), notably hydroxyapatite (HA), are essential biological minerals in natural hard tissues and are integral to bone tissue engineering applications.[1,2] Composite biomaterials for bone tissue engineering often include HA or a Ca-P precursor that can transform into HA under physiological conditions. However, developing a straightforward and scalable method to produce pure HA under mild conditions remains challenging. One promising solution is the "biomimetics" approach, which involves non-classical crystallization through amorphous intermediates. Understanding the formation mechanisms of these apatitic minerals can enhance biomaterials development and pave the way for synthesizing nonbiogenic minerals.[3–5]

Despite extensive research on Ca-P, the precise crystallization pathway of amorphous particles into HA, the mechanisms behind this transformation, and its kinetics are still under investigation. Studies on the nucleation of biological HA concur that HA does not form directly from solution but through an amorphous calcium phosphate (ACP) precursor.[6,7] There is ongoing debate about the factors driving this ACP-mediated process, from ACP formation to its transition to HA. Tang's group suggested a solution-mediated surface nucleation process, where HA forms heterogeneously on ACP, with the transformation rate dependent on the initial ACP amount and calcium activity in solution.[8–13] In contrast, Xie *et al.* and Wang *et al.* proposed that HA nucleation occurs within the ACP through a solid–solid transformation.[14,15]

Different proposed mechanisms for ACP-mediated HA formation suggest varying roles for additives. Additives can stabilize or destabilize ACP by altering its dissolution rate, affect the HA nucleation rate, or influence the chemistry and solubility of the ACP phase, impacting the solution's supersaturation. The presence of biomolecules, such as amino acids, can induce specific polymorph nucleation and affect crystal morphology.[16–19] Sodium trimetaphosphate (STMP), a phosphorylating agent used in the food industry, can also introduce phosphate groups onto collagen surfaces, promoting mineralization.[20,21] Therefore, the choice of biomolecules and

[a]School of Civil Engineering, Shandong Jiaotong University, Ji'nan 250357, China. E-mail: sdzblijin@163.com

[b]Jinan Key Laboratory for Low-Carbon and Eco-Friendly Road Materials, Shandong Jiaotong University, Ji'nan 250357, China

[c]Shanghai Tenth People's Hospital, School of Medicine, Tongji University, Shanghai 200092, China

[d]Shandong Provincial Engineering and Technical Center of Light Manipulations and Shandong Provincial Key Laboratory of Optics and Photonic Device, School of Physics and Electronics, Shandong Normal University, Ji'nan 250014, China. E-mail: yaoshk@sdnu.edu.cn

[e]Collaborative Innovation Center of Light Manipulation and Applications, Shandong Normal University, Ji'nan 250358, China

† Electronic supplementary information (ESI) available. See DOI: https://doi.org/10.1039/d4ra04078c

phosphorus sources is crucial for creating Ca-P particles with desired structures.

This study introduces a one-step hydrothermal synthesis strategy for Ca-P microspheres, utilizing STMP as the phosphorus source and L-glutamic acid as an additive. ACP serves as an intermediate phase that readily transitions as a precursor for HA microsphere growth. By adjusting the reaction time, smooth ACP microspheres can be transformed into porous core–shell HA microspheres. The study investigates the phase evolution, morphology, particle size distribution, BET surface area, and pore size of these core–shell structured HA microspheres over time. The formation mechanism and crystallization process of HA under hydrothermal treatment is discussed, informed by the observed evolution.

2. Experimental

2.1. Materials

The anhydrous calcium chloride ($CaCl_2$, AR), sodium trimetaphosphate ($(NaPO_3)_3$, AR), nitric acid (HNO_3, AR), L-glutamic acid and urea ($CO(NH_2)_2$) were purchased from the Sinopharm Chemical Reagent Company Limited of China (Shanghai, China). All chemical reagents were utilized as received without additional purification.

2.2. Preparation of the samples

Calcium phosphate microspheres were obtained through a hydrothermal route. In a typical step, 0.1 mol per L $CaCl_2$, 0.02 mol per L $(NaPO_3)_3$ and 1 mol per L urea aqueous solutions were first mixed under magnetic stirring. A dilute nitric acid (HNO_3) solution is then used to adjust the pH of the mixture to 3.5 to obtain a clear solution. When the pH of the solution is stable, 0.05 mol per L L-glutamic acid was added to it. The final mixture was hydrothermally treated at 180 °C in a high-pressure reactor lined with Teflon for 0.5, 1, 2, 3 and 8 h, respectively. After the treatment, the products are washed with deionized water and ethanol, centrifuged, and dried.

2.3. Characterizations

The phase composition and functional groups of the samples were examined by powder X-ray diffraction (XRD, Bruker D8 Advance) in the 2θ range of 10–60° and Fourier transform infrared spectroscopy (FTIR, Nicolet IS50) collected between 4000 and 500 cm^{-1}. The crystallite sizes (D_{hkl}) of the three strongest diffraction peak in as-prepared HA products were determined using the Debye–Scherrer approach.[22,23] The degree of crystallinity of the HA samples was calculated by the Jade software. The surface morphologies were characterized using field scanning electron microscope (FE-SEM, Zeiss JSM-7610F) at an acceleration voltage of 5 kV equipped with an energy dispersive spectrometer (EDS) by dropping suspensions onto aluminum foils. The particle size distributions and physical gas adsorption performance were evaluated by laser particle size analyzer (Mastersizer 2000) and Micromeritics ASAP 2460 instrument. Prior to the FE-SEM and PSD tests, the samples were dispersed ultrasonically in anhydrous ethanol for 5 min.

3. Results and discussion

3.1. Phase analysis

The phase composition and functional groups of the synthesized samples were characterized under varying hydrothermal durations using XRD and FTIR spectroscopy, as depicted in Fig. 1. At a hydrothermal duration of 0.5 h, the XRD pattern exhibited a broad and amorphous profile with a prominent peak at $2\theta = 29°$ (Fig. 1a, black line), which is characteristic of the ACP phase.[24] Upon increasing the hydrothermal time to 1 h, the predominant phase remained ACP, albeit with the emergence of several weak diffraction peaks (Fig. 1a, red line). This suggests the onset of crystallization and an impending change in the sample's morphology. Upon further extending the hydrothermal treatment to 2 h, the sample underwent a phase transition to a crystalline HA phase, as evidenced by the XRD pattern which aligns with the standard HA profile (JCPDS 09-0432, shown as the bottom bar chart in Fig. 1a). The three high-intensity diffraction peaks, observed at 2θ values of 31.7°, 32.1°, and 32.9°, are attributed to the crystallographic planes (211), (112), and (300) of the HA phase, respectively. The crystallinity

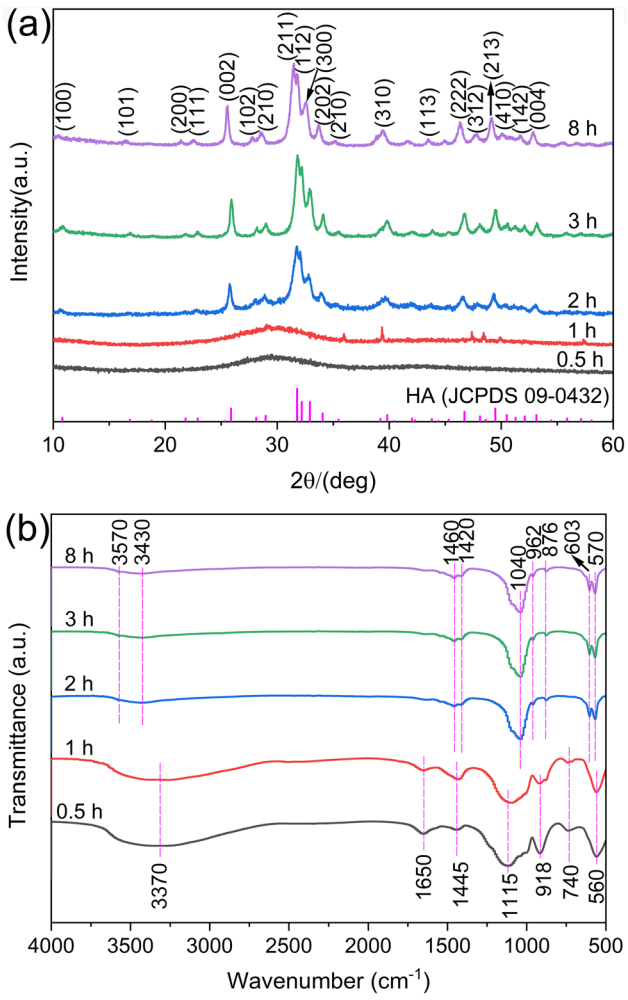

Fig. 1 XRD patterns (a) and FTIR spectra (b) of the samples prepared under different hydrothermal times.

Table 1 The crystallite sizes of D_{hkl} and crystallinity of HA samples synthesized under different hydrothermal times

Hydrothermal treatment time (h)	D_{211} (nm)	D_{112} (nm)	D_{300} (nm)	Crystallinity (%)
2	8.20	19.36	17.52	50.88
3	17.27	22.04	15.67	92.06
8	22.44	15.16	18.66	93.47

of the HA sample significantly enhanced after 3 h of hydrothermal treatment and exhibited minimal further change when the hydrothermal duration was extended to 8 h (Fig. 1a, blue and purple lines). Noticeably, extending the hydrothermal treatment to 8 h, a longer time intervals, aims to explore the stability of the HA sample over an extended period, ensuring that the crystalline phase remains stable and does not undergo further significant changes. This investigation is crucial for understanding the optimal conditions for HA synthesis and its potential applications in various fields.

The crystallographic characteristics for the samples, such as crystallite sizes and crystallinity, are crucial parameters to delve deeper into the crystal growth dynamics.[25] Herein, the D_{hkl} and the degree of crystallinity of HA subjected to varying durations of hydrothermal treatment were measured and are presented in Table 1. The crystallinity, along with the general trend in the growth of crystallite sizes, shows a significant increase, especially when the hydrothermal treatment time is extended from 2 h to 3 h. This suggests that the crystallites grow larger as the treatment time increases, which can be attributed to the prolonged exposure to the hydrothermal conditions that facilitate further crystallization. It is important to note that the calculations for these parameters, as performed using the Jade software, are approximate and should be taken as a reference.

The functional groups of all samples, as revealed by FTIR spectroscopy, substantiate the phase transformation described earlier (refer to Fig. 1b). A distinct peak at 560 cm^{-1} emerges with hydrothermal treatments lasting up to 1 h, indicating the presence of ACP, while the broad absorption peak at 1115 cm^{-1} is a hallmark of ACP (as shown by the black and red lines in Fig. 2b).[26] The peaks at 918 cm^{-1} and 560 cm^{-1} correspond to the stretching and bending vibrational modes of the P–O bonds in the PO_4^{3-} group, respectively. As the hydrothermal duration extends beyond 2 h, the spectral patterns of the samples remain consistent (as indicated by the blue, green, and purple lines in Fig. 2b). The broad peaks at 3430 cm^{-1}, 3370 cm^{-1}, and 1650 cm^{-1} are characteristic of the hydroxyl (OH^-) group present in water molecules. The peak at 3570 cm^{-1} is associated with the stretching vibrations of OH^- within the HA structure, which suggests that the HA crystal lattice remains intact within the sample. The solitary peak at 1445 cm^{-1} is indicative of the characteristic vibration of CO_3^{2-} ions, a product of urea hydrolysis. The broad and weakly defined doublet bands at 1460 cm^{-1} and 1420 cm^{-1}, along with the peak at 876 cm^{-1}, are aligned with the characteristic vibrations of the CO_3^{2-} group. This suggests that CO_3^{2-} ions are substituting for the B-site in the PO_4^{3-} group within HA.[27] It is a well-documented phenomenon for CO_3^{2-} to replace PO_4^{3-} in HA during urea hydrolysis, particularly at temperatures exceeding 80 °C.[28] The peaks around 1040 cm^{-1}, 962 cm^{-1}, 603 cm^{-1}, and 570 cm^{-1} are assigned to the PO_4^{3-} group present in HA.[22] These findings are congruent with the XRD patterns and collectively confirm that the synthesized HA samples are indeed carbonate-substituted HA.

3.2. Morphological characterization

The morphological evolution of the porous HA microspheres was investigated over time using FE-SEM, as illustrated in Fig. 2. At a hydrothermal duration of 0.5 h, the precipitated ACP phases are observed to be spherical with a smooth surface, ranging in size from 1 to 5 μm (Fig. 2a–c). The dimensions of the ACP particles are influenced by several factors, including the solution pH, the concentration of the mixed reagents, and the preparation temperature.[29] Upon increasing the hydrothermal time to 1 h, the morphology of the microspheres undergoes a noticeable change, characterized by the emergence of a small number of particles on the surface and a slight reduction in the microsphere diameter (Fig. 2d–f). Notably, the surface of the microspheres becomes pitted and loses its smoothness. These morphological changes are in agreement with the XRD results. As the hydrothermal time extends to 3 h, the particles continue to grow and accumulate, forming a spherical shell with a discernible gap from the inner core, leading to the formation of HA core–shell microspheres with a diameter of approximately 2 μm (Fig. 2g–i). In some instances, the nuclei have begun to separate from the shell. The transformation from ACP to crystalline HA phase is suggested to occur through nucleation and/or the direct formation of crystalline phases within the ACP phases or on their surface, followed by outward growth *via* the Kirkendall process, with the internal ACP phases supplying the material flux necessary for phase conversion.[30] Further extending the hydrothermal time to 8 h results in the HA maintaining a core–shell microsphere morphology (Fig. 2j and k). It is observed that the microspheres, post-core–shell separation, exhibit a porous structure (Fig. 2l). With prolonged hydrothermal treatment, the reaction becomes more complete, and the microspheres exhibit enhanced stability.

Upon closer examination, it is observed that the synthesized HA core–shell microspheres are composed of an inner core and an outer shell (Fig. 3a). The shell is constructed from nano whiskers, which measure approximately 200–800 nm in length, and there are discernible gaps between the core and the shell, as shown in Fig. 3a–c. In certain regions, the core has become entirely detached from the shell, as depicted in Fig. 3d.

To substantiate the transformation process from ACP to HA, element analysis of the samples prepared for 0.5 h and 2 h was conducted using EDS. As depicted in Fig. 4, S1 and 2 (ESI),† the presence of calcium (Ca), phosphorus (P), and oxygen (O) is observed in both the ACP and HA microspheres. The detection of aluminum (Al) and platinum (Pt) is attributed to the use of aluminum foil during sample preparation. A notable increase in the Ca/P atomic ratio is observed, rising from 1.034 to 1.642 as calculated from the EDS spectrum curves. This increase aligns

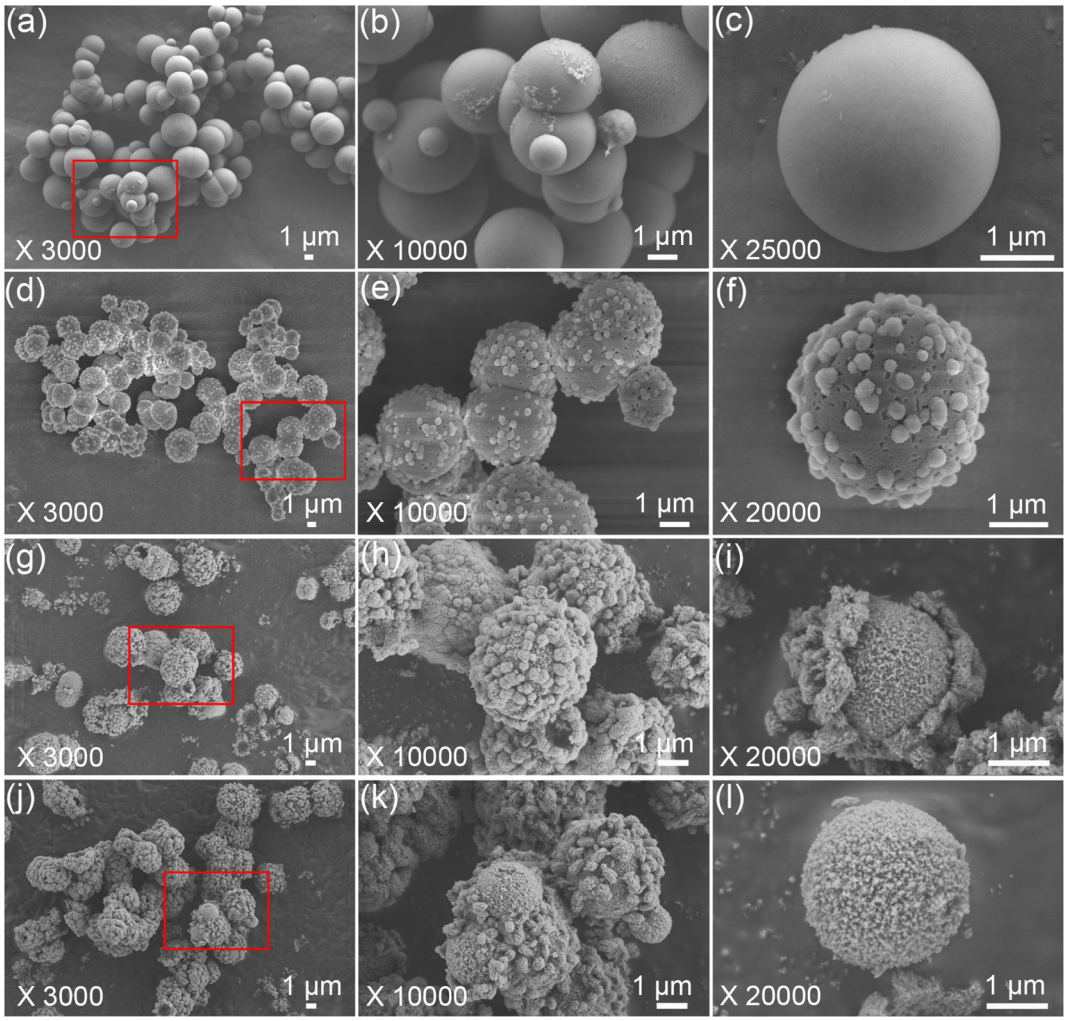

Fig. 2 FE-SEM images of the products prepared under different hydrothermal times. (a–c) 0.5 h, (d–f) 1 h, (g–i) 3 h and (j–l) 8 h. (b), (e), (h), and (k) in the second column are high-magnification views of the areas within the red rectangular boxes in (a), (d), (g), and (j), respectively.

with the expected chemical transformation from ACP to HA. It is noteworthy that ACP can be synthesized with a Ca/P molar ratio as low as approximately 1.0,[31–33] whereas the stoichiometric ratio for HA is 1.67.

3.3. Particle size distribution and specific surface area

The particle size distribution and physical gas adsorption properties are pivotal in determining the characteristics of synthesized microspheres. Granulometric analysis data for ACP and HA microspheres, prepared under varying hydrothermal conditions, are detailed in Fig. 5 and Table 2. The particle size distribution curves, as shown in Fig. 5, reveal that both types of microspheres have a concentrated size distribution, adhering to a Gaussian pattern, with two main size peaks suggesting uniformity in microsphere sizing. The observed shift from larger to smaller diameters marks the transition from solid ACP to core–shell HA microspheres, a finding corroborated by FE-SEM analysis, indicating that there is a sign of ACP shrinkage during HA growth. Notably, the particle size within the 3–10 μm range remains stable over hydrothermal treatments ranging from 3 to 8 h, indicating minimal alteration in HA microsphere size with extended treatment duration. Table 1 further illustrates that while the mean particle size decreases from 9.26 μm to approximately 5.72 μm as the hydrothermal treatment time increases from 0.5 to 3 h, there is a negligible change in mean particle size with additional treatment extending to 8 h.

Fig. 6a illustrates the nitrogen adsorption–desorption isotherms for microspheres synthesized under varying hydrothermal durations. These isotherms, along with their type H3 hysteresis loops, are categorized as type IV according to the International Union of Pure and Applied Chemistry (IUPAC). This classification is indicative of a shell that self-assembles from clusters, creating slit-shaped pores. As depicted in Fig. 6b, the pore width distributions widen with increasing hydrothermal time, suggesting that more intricate pore channels are beneficial for drug loading and sustained release. Table 3 compiles the BET surface areas, total pore volumes, and average pore diameters for microspheres produced at different hydrothermal times of 0.5, 1, and 3 h. Initially, at a hydrothermal time of 0.5 h, the ACP microspheres exhibit a relatively

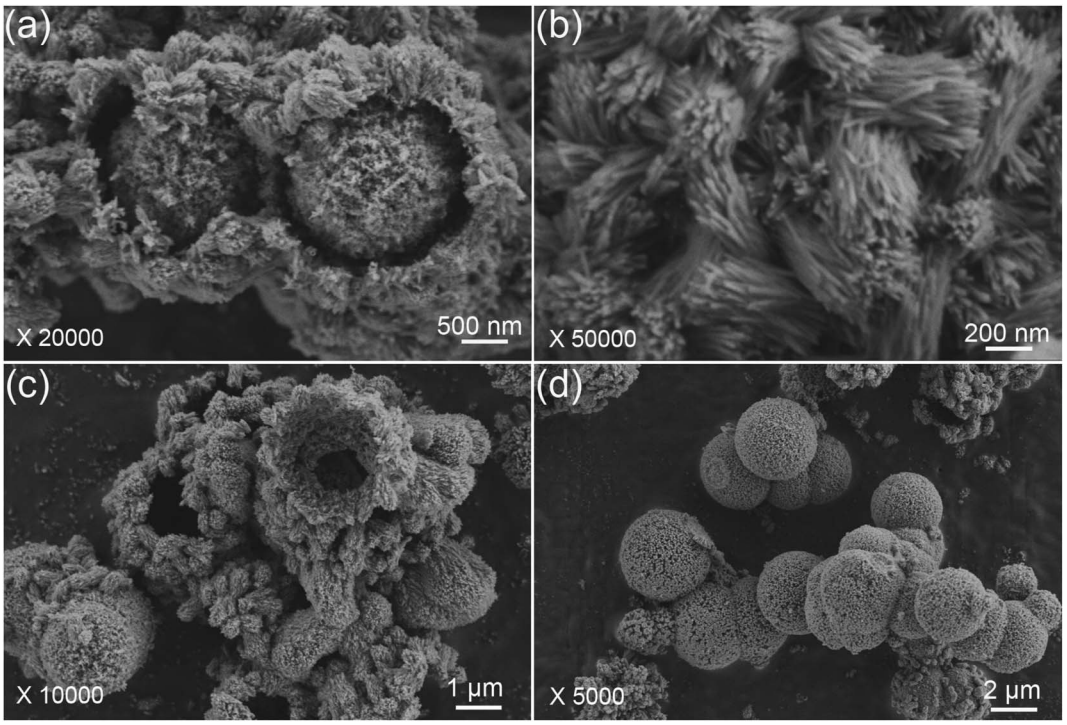

Fig. 3 FE-SEM images of the core–shell HA microspheres after broken. (a) Core–shell microspheres, (b) high magnification of the outer shells in (a), (c) hollow exterior shells and (d) isolated inner cores separated from the core–shell structure.

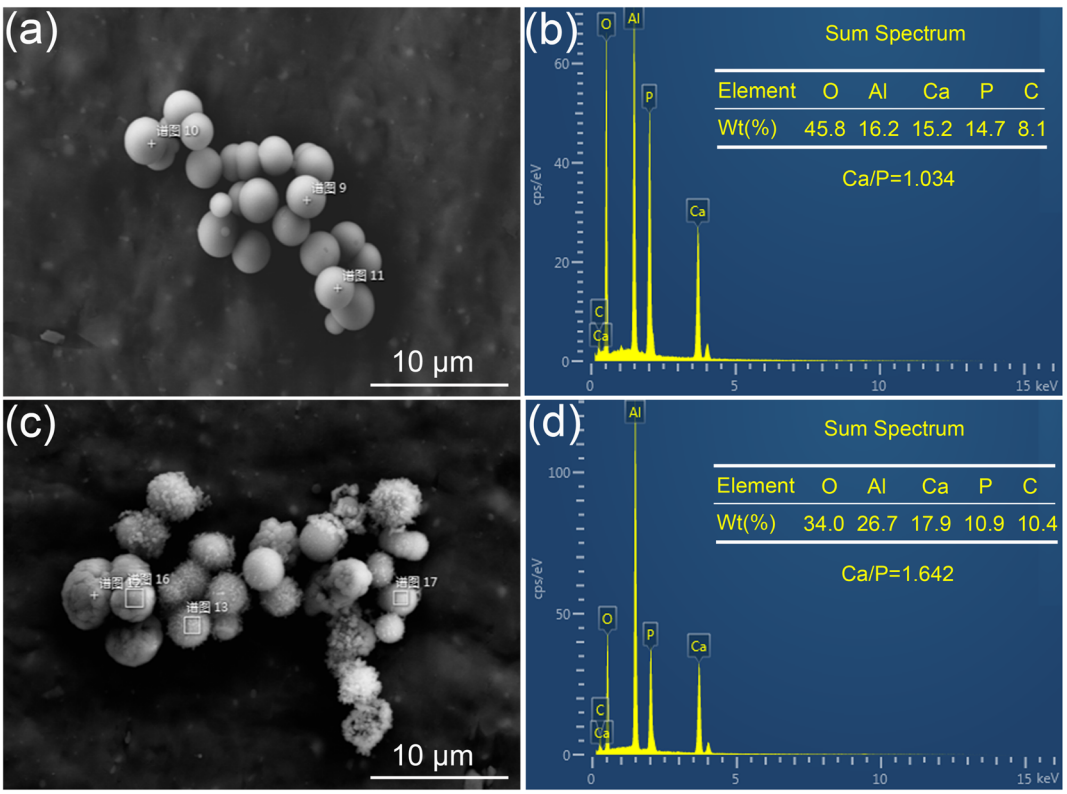

Fig. 4 Electronic images and corresponding EDS spectra of the products prepared under different hydrothermal times. (a and b) 0.5 h and (c and d) 2 h.

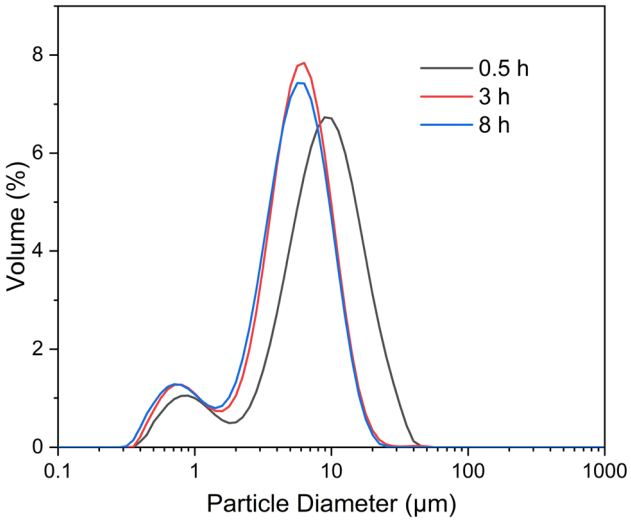

Fig. 5 Particle size distribution curves of the microspheres prepared under different hydrothermal treatment times.

Table 2 Particle sizes of the synthesized microspheres[a]

Hydrothermal treatment time (h)	$d_{0.1}$ (μm)	$d_{0.5}$ (μm)	$d_{0.9}$ (μm)	Mean size (μm)
0.5	1.83	7.96	17.95	9.26
1	1.21	5.18	10.32	5.72
3	1.09	4.93	10.03	5.44

[a] $d_{0.1}$, $d_{0.5}$ and $d_{0.9}$ means 10%, 50% and 90% of total particle size less than some value, respectively.

low BET surface area of 3.00 m^2 g^{-1}. This specific surface area progressively increases to 5.17 m^2 g^{-1} as the hydrothermal time is extended. Notably, the HA microspheres, once the core–shell structure is established, exhibit a significantly higher BET surface area of 35.24 m^2 g^{-1}. This elevated surface area can be ascribed to the porous structure and the self-assembly of nano whiskers that serve as the building blocks for the external shell, which is characteristic of a typical mesoporous structure.[34] The average Barrett–Joyner–Halenda (BJH) pore size for the solid ACP microspheres is 7.24 nm, whereas for the HA core–shell microspheres, it expands to 14.91 nm. All the characteristic makes them an exemplary candidate for drug-delivery systems, presenting a strong potential in the realms of controlled drug release and targeted therapeutics.

3.4. From smooth ACP to core–shell HA: a proposed growth mechanism of the microspheres

The ACP-to-HA conversion in this experiment is a complex, multi-step process, with the structural evolutions depicted in Fig. 7.

3.4.1 Nucleation and initial formation. The process initiates with urea hydrolysis, which releases OH^-, creating an alkaline environment. This environment facilitates the conversion of $P_3O_{10}^{5-}$ to OH– PO_4^{3-}. As the concentration of Ca^{2+} and PO_4^{3-} ions in the solution reaches supersaturation, Ca–P clusters form, which are the precursors to ACP.

3.4.2 Role of glutamic acid. Glutamic acid plays a crucial role by chelating with calcium ions, promoting the aggregation of ions and the formation of Ca–P clusters. The charged side chain of glutamic acid is instrumental in the growth of these clusters, although it does not become part of the clusters.[35]

3.4.3 Formation of ACP microspheres. Posner's clusters, fundamental units of ACP, are pivotal to apatite nucleation in solution.[36,37] ACP microspheres form due to surface characteristics during hydrothermal reactions, with higher supersaturation leading to smaller microspheres.

3.4.4 Transformation to HA. ACP, Being metastable, is more soluble than the stable HA and tends to transform into other calcium phosphate phases.[38,39] The $P_3O_{10}^{5-}$ can chelate with Ca^{2+} on the ACP surface, creating active nucleation sites for whisker-like apatite to nucleate and grow through a dissolution–reprecipitation mechanism.[40]

3.4.5 Core–shell structure development. As the hydrothermal process continues, the internal ACP microspheres slightly dissolve, while external nanoclusters accumulate to

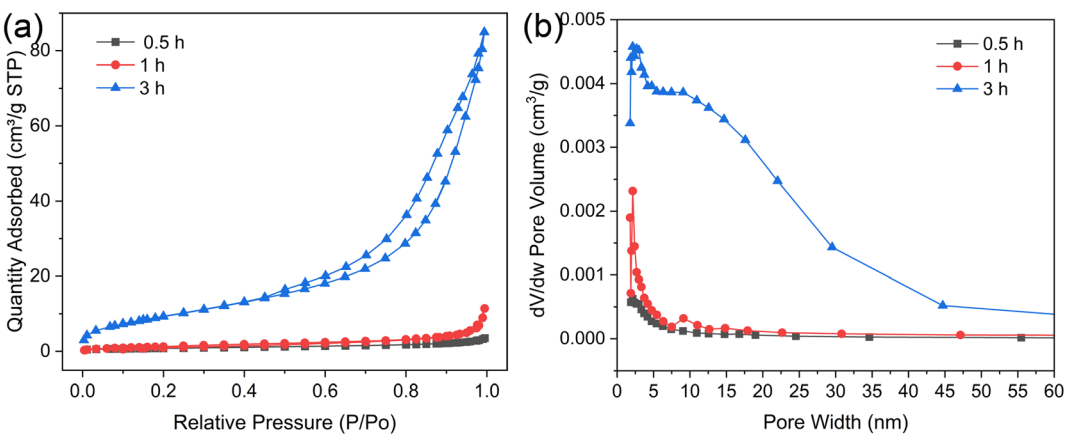

Fig. 6 Physical gas adsorption performance analysis of the microspheres prepared under different hydrothermal times. (a) N_2 adsorption–desorption isotherms and (b) BJH desorption pore size distribution curves.

Table 3 BET surface areas, total pore volumes and average pore diameters of the synthesized microspheres

Hydrothermal treatment time (h)	BET surface area (m^2 g^{-1})	Total pore volume (cm^3 g^{-1})	Average pore diameter (nm)
0.5	3.00	0.0054	7.24
1	5.17	0.0177	13.69
3	35.24	0.1314	14.91

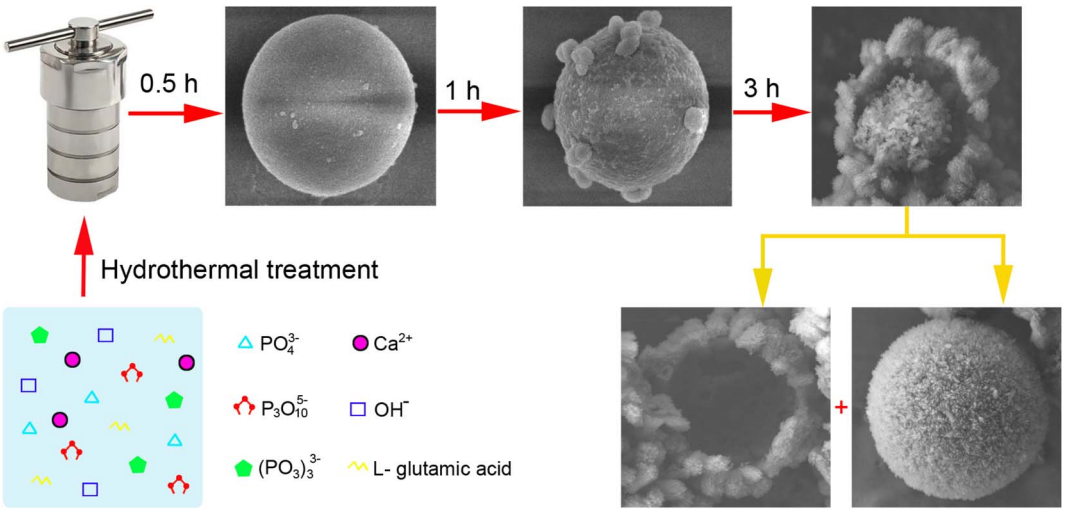

Fig. 7 Formation mechanism of the HA microspheres transformed from ACP.

form a porous shell, creating a gap from the internal microspheres.

3.4.6 Phase transition mechanism. The internal ACP microspheres gradually transform into HA crystals, forming the core. The internal microspheres' phase transition is likely a surface-mediated transformation, where surface dissolution promotes ion migration for HA nucleation and growth. The reorganization of Posner's clusters into HA crystals within the core requires minimal activation energy, facilitating the transformation.[41]

3.4.7 Final product. The end result is pure HA microspheres with a core–shell structure, where the shell is composed of porous HA nanoclusters and the core is crystalline HA.

This transformation process is significant for applications in biomaterials and drug delivery, as it results in microspheres with unique properties that can be tailored for specific uses, such as controlled drug release and bone growth promotion.

4. Conclusions

In summary, porous HA microspheres featuring a core–shell structure have been successfully synthesized from smooth ACP microspheres by using sodium trimetaphosphate and L-glutamic through a one-step hydrothermal method. A time-gradient experiment elucidated the progression from smooth to core–shell microspheres, along with the phase transition from ACP to HA. When subjected to hydrothermal conditions exceeding 3 h, pure core–shell HA microspheres with enhanced crystallinity, an average diameter of 5.44 μm, and a BET surface area of 35.24 m^2 g^{-1} were obtained. A plausible mechanism for the crystallization of smooth ACP microspheres into core–shell HA microspheres has been proposed, involving a multi-step reaction with sodium trimetaphosphate and a dissolution–recrystallization process during nucleation and growth. These findings provide valuable insights into a pivotal yet previously obscure phase in the formation of HA crystals, particularly within the context of hydrothermal synthesis.

Data availability

The authors confirm that the data supporting the findings of this study are available within the article and the ESI.†

Conflicts of interest

The authors declare that they have no conflicts of interest.

Acknowledgements

This study was supported by the Young Talent of Lifting Engineering for Science and Technology in Shandong, China (Award No. SDAST2021qt05), Shandong Provincial Natural Science Foundation (Award No. ZR2020QE070, ZR2020QA076 and ZR2021MB128) and the National Key R&D Program of China (2022YFB2601900).

References

1 S.-D. Jiang, Q.-Z. Yao, Y.-F. Ma, G.-T. Zhou and S.-Q. Fu, Phosphate-dependent morphological evolution of hydroxyapatite and implication for biomineralisation, *Gondwana Res.*, 2015, **28**(2), 858–868.

2 S. K. Avinashi, Shweta, B. Bohra, R. K. Mishra, S. Kumari, Z. Fatima, A. Hussain, B. Saxena, S. Kumar, M. Banerjee and C. R. Gautam, Fabrication of Novel 3-D Nanocomposites of HAp–TiC–h-BN–ZrO_2: Enhanced Mechanical Performances and In Vivo Toxicity Study for Biomedical Applications, *ACS Biomater. Sci. Eng.*, 2024, **10**(4), 2116–2132.

3 M. L. Oyen, The materials science of bone: Lessons from nature for biomimetic materials synthesis, *MRS Bull.*, 2008, **33**(1), 49–55.

4 J. Aizenberg, D. A. Muller, J. L. Grazul and D. Hamann, Direct fabrication of large micropatterned single crystals, *Science*, 2003, **299**(5610), 1205–1208.

5 D. C. Bassett, L. M. Grover, F. A. Müller, M. D. McKee and J. E. Barralet, Serum protein controlled nanoparticle synthesis, *Adv. Funct. Mater.*, 2011, **21**(15), 2968–2977.

6 S. Weiner, J. Mahamid, Y. Politi, Y. Ma and L. Addadi, Overview of the amorphous precursor phase strategy in biomineralization, *Front. Mater. Sci. China*, 2009, **3**, 104–108.

7 M. Sawada, K. Sridhar, Y. Kanda and S. Yamanaka, Pure hydroxyapatite synthesis originating from amorphous calcium carbonate, *Sci. Rep.*, 2021, **11**(1), 11546.

8 H. Ding, H. Pan, X. Xu and R. Tang, Toward a detailed understanding of magnesium ions on hydroxyapatite crystallization inhibition, *Cryst. Growth Des.*, 2014, **14**(2), 763–769.

9 S. Jiang, Y. Chen, H. Pan, Y.-J. Zhang and R. Tang, Faster nucleation at lower pH: amorphous phase mediated nucleation kinetics, *Phys. Chem. Chem. Phys.*, 2013, **15**(30), 12530–12533.

10 S. Jiang, H. Pan, Y. Chen, X. Xu and R. Tang, Amorphous calcium phosphate phase-mediated crystal nucleation kinetics and pathway, *Faraday Discuss.*, 2015, **179**, 451–461.

11 Z. Guo, Z. Liu and R. Tang, Applications of amorphous inorganics as novel functional materials, *Mater. Chem. Front.*, 2024, **8**(7), 1703–1730.

12 Y. Xiao, J. Lin, Y. Zhao, X. Wang, Q. Lv, W. Li, R. Tang and G. Fu, Plaque-Specific Adhesive Balloons Coated with Calcium Phosphate Nanoparticles Loaded with Rapamycin for Atherosclerosis Therapy, *Adv. Funct. Mater.*, 2024, 2315317.

13 B. Jin, Z. Liu, C. Shao, J. Chen, L. Liu, R. Tang and J. J. De Yoreo, Phase transformation mechanism of amorphous calcium phosphate to hydroxyapatite investigated by liquid-cell transmission electron microscopy, *Cryst. Growth Des.*, 2021, **21**(9), 5126–5134.

14 B. Xie, T. J. Halter, B. M. Borah and G. H. Nancollas, Tracking amorphous precursor formation and transformation during induction stages of nucleation, *Cryst. Growth Des.*, 2014, **14**(4), 1659–1665.

15 C.-G. Wang, J.-W. Liao, B.-D. Gou, J. Huang, R.-K. Tang, J.-H. Tao, T.-L. Zhang and K. Wang, Crystallization at multiple sites inside particles of amorphous calcium phosphate, *Cryst. Growth Des.*, 2009, **9**(6), 2620–2626.

16 M.-L. Qi, J. Qi, G.-Y. Xiao, K.-Y. Zhang, C.-Y. Lu and Y.-P. Lu, One-step hydrothermal synthesis of carbonated hydroxyapatite porous microspheres with a large and uniform size regulated by l-glutamic acid, *CrystEngComm*, 2016, **18**(31), 5876–5884.

17 M. Tavafoghi and M. Cerruti, The role of amino acids in hydroxyapatite mineralization, *J. R. Soc., Interface*, 2016, **13**(123), 20160462.

18 Z. Li, Q. Ren, J. Cui, D. Hu, T. Tian, T. He, K. Wang, W. Jiang and L. Zhang, Comparing the efficacy of hydroxyapatite nucleation regulated by amino acids, poly-amino acids and an amelogenin-derived peptide, *CrystEngComm*, 2020, **22**(22), 3814–3823.

19 Z. Wang, Z. Xu, W. Zhao and N. Sahai, A potential mechanism for amino acid-controlled crystal growth of hydroxyapatite, *J. Mater. Chem. B*, 2015, **3**(47), 9157–9167.

20 W.-L. Xu, B. Liu, Y.-C. Wang, G.-Y. Xiao, X. Chen, W.-H. Xu and Y.-P. Lu, A facile strategy for one-step hydrothermal preparation of porous hydroxyapatite microspheres with core–shell structure, *J. Mater. Res. Technol.*, 2022, **17**, 320–328.

21 M.-L. Qi, S. Qin, Y.-C. Wang, S. Yao, L. Qi, Y. Wu, Y.-P. Lu and F. Cui, Controlled synthesis of hydroxyapatite nanomaterials regulated by different phosphorus sources, *Crystals*, 2020, **10**(8), 678.

22 Y.-C. Wang, Z.-C. Wang, G.-Y. Xiao, W.-L. Xu, K. Wang, Y. Jiao, M.-L. Qi and Y.-P. Lu, Investigation on $[OH^-]$ responsive systems for construction of one-dimensional hydroxyapatite via a solvothermal method, *New J. Chem.*, 2021, **45**(1), 358–364.

23 J. Jana, T. S. K. Sharma, J. S. Chung, W. M. Choi and S. H. Hur, Role of Physicochemical Features toward Bifunctional Redox Activity of Transition-Metal Molybdates, *ACS Sustain. Chem. Eng.*, 2023, **11**(35), 13013–13023.

24 S. V. Dorozhkin, Synthetic amorphous calcium phosphates (ACPs): Preparation, structure, properties, and biomedical applications, *Biomater. Sci.*, 2021, **9**(23), 7748–7798.

25 T. S. K. Sharma, *et al.*, Rational synthesis of alkaline earth metal vanadates: Structural origin of MgVO3 honeycomb lattice system and its electrochemical analysis for the detection of sulfadiazine, *Chem. Eng. J.*, 2023, **464**, 142673.

26 S. Gadaleta, E. Paschalis, F. Betts, R. Mendelsohn and A. Boskey, Fourier transform infrared spectroscopy of the solution-mediated conversion of amorphous calcium phosphate to hydroxyapatite: new correlations between X-ray diffraction and infrared data, *Calcif. Tissue Int.*, 1996, **58**, 9–16.

27 M. Vignoles, G. Bonel, D. Holcomb and R. Young, Influence of preparation conditions on the composition of type B carbonated hydroxyapatite and on the localization of the carbonate ions, *Calcif. Tissue Int.*, 1988, **43**, 33–40.

28 S. P. Parthiban, I. Y. Kim, K. Kikuta and C. Ohtsuki, Effect of urea on formation of hydroxyapatite through double-step hydrothermal processing, *Mater. Sci. Eng., C*, 2011, **31**(7), 1383–1388.

29 N. Blumenthal, A. Posner and J. Holmes, Effect of preparation conditions on the properties and transformation of amorphous calcium phosphate, *Mater. Res. Bull.*, 1972, **7**(11), 1181–1189.

30 J. Tao, H. Pan, J. Wang, J. Wu, B. Wang, X. Xu and R. Tang, Evolution of amorphous calcium phosphate to hydroxyapatite probed by gold nanoparticles, *J. Phys. Chem. C*, 2008, **112**(38), 14929–14933.

31 Z. Zyman, A. Goncharenko and D. Rokhmistrov, Kinetics and mechanisms of the transformation of precipitated amorphous calcium phosphate with a Ca/P ratio of 1: 1 to calcium pyrophosphates, *J. Cryst. Growth*, 2017, **478**, 117–122.

32 Z. Zyman, M. Epple, A. Goncharenko, D. Rokhmistrov, O. Prymak and K. Loza, Thermally induced crystallization and phase evolution in powders derived from amorphous calcium phosphate precipitates with a Ca/P ratio of 1: 1, *J. Cryst. Growth*, 2016, **450**, 190–196.

33 Z. Zyman, M. Epple, A. Goncharenko, D. Rokhmistrov, O. Prymak and K. Loza, Peculiarities in thermal evolution of precipitated amorphous calcium phosphates with an initial Ca/P ratio of 1: 1, *J. Mater. Sci.: Mater. Med.*, 2017, **28**, 1–7.

34 R. Pierotti and J. Rouquerol, Reporting physisorption data for gas/solid systems with special reference to the determination of surface area and porosity, *Pure Appl. Chem.*, 1985, **57**(4), 603–619.

35 Z. Xue, M. Yang and D. Xu, Nucleation of biomimetic hydroxyapatite nanoparticles on the surface of type I collagen: molecular dynamics investigations, *J. Phys. Chem. C*, 2019, **123**(4), 2533–2543.

36 M. W. Swift, C. G. Van de Walle and M. P. Fisher, Posner molecules: from atomic structure to nuclear spins, *Phys. Chem. Chem. Phys.*, 2018, **20**(18), 12373–12380.

37 A. S. Posner and F. Betts, Synthetic amorphous calcium phosphate and its relation to bone mineral structure, *Acc. Chem. Res.*, 1975, **8**(8), 273–281.

38 S. V. Dorozhkin, *Calcium Orthophosphate-Based Bioceramics and Biocomposites*, John Wiley & Sons, 2016.

39 S. V. Dorozhkin, Amorphous calcium orthophosphates: nature, chemistry and biomedical applications, *Int. J. Mater. Chem.*, 2012, **2**(1), 19–46.

40 E. D. Eanes, Amorphous calcium phosphate, *Octacalcium phosphate*, 2001, vol. 18, pp. 130–147.

41 F. Abbona and A. Baronnet, A XRD and TEM study on the transformation of amorphous calcium phosphate in the presence of magnesium, *J. Cryst. Growth*, 1996, **165**(1–2), 98–105.